Nuclear charge densities with the Skyrme Hartree-Fock method

W. A. Richter
Department of Physics, University of Stellenbosch, Stellenbosch 7600, South Africa

B. A. Brown
Department of Physics and Astronomy, and National Superconducting Cyclotron Laboratory, Michigan State University, East Lansing, Michigan 48824-1321

(Received 12 August 2002; published 25 March 2003)

Charge-density distributions and the associated nuclear radii are calculated with the Hartree-Fock method for comparison with available data from electron scattering. Two forms of Skyrme interactions are used for the calculations. As a further refinement the single-particle occupancies are constrained to values obtained from shell-model calculations. A significant improvement in the agreement is obtained if shell-model occupancies are used.

DOI: 10.1103/PhysRevC.67.034317 PACS number(s): 21.10.Ft, 21.60.Cs, 21.60.Jz

I. INTRODUCTION

Elastic electron scattering from nuclei has provided a great resource of experimental data with which to test models for nuclear ground states. It evolved from the early determinations of rms charge radii, to much more precise measurements in the 1970s and 1980s, which have provided nearly model-independent determinations of the charge-density distributions of many nuclei [1,2]. In these density distributions one can observe oscillations in the interior density, which represent the quantum ''waves'' in the nucleus. In this paper we compare the experimental data for the charge form factors and the associated charge densities in a wide range of nuclei to those obtained in modern theoretical formulations based on the spherical shell model.

The charge densities are based on the point densities for the protons and neutrons obtained in the spherical shell-model basis:

$$\rho(r)_{p/n}=\sum_{n,\ell,j} n_{n,\ell,j,p/n}\rho(r)_{n,\ell,j,p/n}, \qquad (1)$$

where $n_{n,\ell,j}$ are the occupation numbers for each orbital, and $\rho(r)_{n,\ell,j}$ are the single-particle densities for each orbital. For closed-shell configurations, $n_{n,\ell,j}=(2j+1)$ for the occupied orbits and 0 for the unoccupied orbits. The charge density is obtained from the point proton and neutron distributions by folding with the charge densities of the proton and neutron, and are corrected for spurious center-of-mass motion and for the spin-orbit charge density as described in Ref. [3]. The shape of the charge-density distribution is mainly determined by the shape of the point-proton density.

Most of the comparison with data will be made with single-particle densities obtained with Skyrme Hartree-Fock calculations. These are self-consistent calculations in the sense that the potential from which the single-particle densities are calculated depends upon a functional of the total proton and neutron densities from Eq. (1), together with those for the kinetic energy and spin-orbit densities. For comparison we will also show some results based on the single-particle densities obtained from the non-self-consistent Woods-Saxon potential.

For many nuclei away from the closed shells, the occupation numbers can be obtained from configuration mixing shell-model calculations in a model space that spans the orbitals between the magic numbers. For the nuclei covered in this review we use the following model spaces and Hamiltonians: For ^{12}C we use the PJT Hamiltonian [4] in the $(0p_{3/2},0p_{1/2})$ model space. For the sd-shell nuclei ($A=28$–36) we use the USD Hamiltonian [5] in the $(0d_{5/2},0d_{3/2},1s_{1/2})$ model space. For the pf-shell nuclei ($A=48$–65) we use the FPD6 pf-shell Hamiltonian [6] in the $(0f_{7/2},0f_{5/2},1p_{3/2},1p_{1/2})$ model space. For nuclei with $N=50$ we use the Ji-Wildenthal Hamiltonian [7] for protons in the $(0f_{5/2},1p_{3/2},1p_{1/2},0g_{9/2})$ model space, and for ^{204}Hg we use the modified Kuo-Herrling interaction [8] in the model space for the major shells below ^{208}Pb. ^{208}Pb is always assumed to be a closed shell.

To observe the effect of configuration mixing we will make some comparisons between the results obtained with the extreme single-particle (ESP) filling of the spherical orbitals and those obtained with the fractional occupations that result from the shell-model configuration mixing (CM). The self-consistent Hartree-Fock calculations are carried out with the densities in Eq. (1) obtained with the ESP or CM (fractional) orbit occupations.

For the Skyrme Hamiltonian we choose two parameter sets that give good agreement for the nuclear rms radii and binding energies, but which are different enough to give some variety in the calculated charge densities. These are SKX_{csb}, Ref. [9], and SKM*, Ref. [10]. The recent SKX_{csb} Hamiltonian is based on the SKX Hamiltonian [11] with a charge-symmetry-breaking (CSB) interaction added to account for the nuclear displacement energies [9] (the binding energy differences of mirror nuclei). In the original SKX Hamiltonian, a CSB Hamiltonian was effectively implemented by leaving out the Coulomb-exchange part of the Hamiltonian. The charge densities obtained from SKX and SKX_{csb} are essentially identical, and the SKX_{csb} results will be referred to as the ''SKX'' in the remainder of the paper. One ingredient that distinguishes SKX from other Skyrme

interactions is the emphasis on reproducing the single-particle energies near the doubly magic nuclei. Altogether 79 single-particle energies are included in the data set for fitting the parameters of the Skyrme Hamiltonian.

The SKX Hamiltonian uses $\alpha=1/2$ for the power in the density-dependent part of the Hamiltonian, $[\rho(r)]^{\alpha}$. In the SKX fit, lower powers of the density were explored, as in the SKX_m of Ref. [11], where $\alpha=1/3$; but the optimal results for the single-particle spectrum of heavy nuclei were obtained with $\alpha=1/2$. If one puts less emphasis on single-particle energies, a wider range of α values is allowed, with the smallest value of $\alpha=1/6$ found in the SKM* interaction. This change in density dependence from $\alpha=1/2$ to $\alpha=1/6$ has an influence on the charge density, which we will discuss. α has a strong influence on the incompressibility coefficient of symmetric nuclear matter with values of $K=270$ MeV for SKX and $K=216$ MeV for SKM*.

Our Skyrme Hartree-Fock results (and most others in the literature) are with respect to a nuclear shell-model truncation where nuclei such as ^{208}Pb have a closed-shell configuration, and where nuclei between the magic numbers are described by configuration mixing within the valence shell (e.g., the set of orbitals between magic numbers). From one-proton knock-out experiments such as $(e,e'p)$, the absolute spectroscopic factors are found to be reduced by factors of 0.6–0.8 over those expected from the closed-shell configuration [12]. Thus one would infer that the actual nucleonic wave function for ^{208}Pb is much more complex than that of a closed-shell configuration. Indeed, it is well known that the effect of dynamical correlations in the ground states of closed-shell nuclei is important [13]. With the Skyrme interactions one attempts to describe these ground-state correlations in terms of an effective mean field appropriate for a closed-shell configuration. The success of this approach might be justified in the framework of the density-functional models that have been widely used in atomic, molecular, and condensed matter physics [14].

In Ref. [11] the charge densities obtained with SKX for ^{208}Pb, ^{90}Zr, and ^{48}Ca were compared to experiment. The detailed agreement in shape was very good even though only the rms charge radii for these nuclei in the data set were used to determine the parameters. The purpose of the present work is to examine a much wider set of nuclei and to discuss to what extent further improvements are possible within the functional form provided by the Skyrme Hamiltonian.

II. GENERAL FEATURES OF THE CALCULATIONS

In this paper we are primarily concerned with properties of the ground-state charge density $\rho(r)_{ch}$, which gives the most direct physical insight into the distribution of protons inside the nucleus. The charge-density normalization is given by

$$4\pi\int \rho(r)_{ch} r^2\, dr = Z, \tag{2}$$

where Z is the number of protons in the nucleus. The charge probability density

$$P(r)_{ch} = 4\pi r^2 \rho(r)_{ch} \tag{3}$$

represents the probability to find Z protons at a given radius r from the center of the nucleus.

Electron scattering cross sections as a function of momentum transfer q are related to the plane-wave Fourier transform of the charge density:

$$F(q) = \frac{1}{Z}\int \rho(r)_{ch} e^{i\vec{q}\cdot\vec{r}} d\tau = \frac{4\pi}{Z}\int \rho(r)_{ch} j_o(qr) r^2 dr, \tag{4}$$

where $j_o(qr)=\sin(qr)/qr$. The normalization in Eq. (4) is chosen to give $F(q=0)=1$. For light nuclei the electron energy distortion is small, and the cross section is closely proportional to the form factor $|F(q)|^2$ which has minima corresponding to the zeros of $F(q)$. For heavy nuclei the electron energy distortion is larger, and the minima in the cross sections are washed out. From a distorted wave Born approximation (DWBA) analysis of the electron scattering cross section, one can extract $F(q)$ with good precision over the range of momentum transfers measured.

From the measured form factors one can obtain the charge density with the inverse of Eq. (4):

$$\rho(r)_{ch} = \frac{Z}{2\pi^2}\int F(q) j_o(qr) q^2 dq. \tag{5}$$

Since the form factor data are only determined up to some q_{max}, the resulting charge density has some ''error band'' that depends upon the assumptions made about $F(q)$ for $q > q_{max}$.

For our comparisons we make use of the large set of nuclei for which a Fourier-Bessel expansion fit [15] was made to the electron scattering data [1,2]. The Fourier-Bessel expansion is given by

$$\rho(r)_{ch} = \sum_{\nu=1}^{n_{max}} a_\nu j_o(\nu\pi r/R) \tag{6}$$

for $r \leqslant R$ and $\rho(r)_{ch}=0$ for $r>R$, with the associated plane-wave transform

$$F(q) = \frac{4\pi}{Z}\frac{(qR)^2}{\nu q^3}\sum_{\nu=1}^{n_{max}} \alpha_\nu [j_o(\nu\pi - qR) - j_o(\nu\pi + qR)]. \tag{7}$$

The parameters a_ν, ν_{max}, and R are given in Refs. [1,2].

The experimental errors are not given in Refs. [1,2], and we do not attempt to show an experimental ''error band'' for the charge densities, the size of which is strongly correlated with q_{max}. In a few cases, more than one data set is used and a comparison of these in the figures for the charge densities gives an indication of the error. General aspects of the statistical and model-dependent errors in these Fourier-Bessel fits are discussed by Dreher *et al.* [15], and those related to specific experiments are discussed in the original experimental papers. Generally the width of the error band

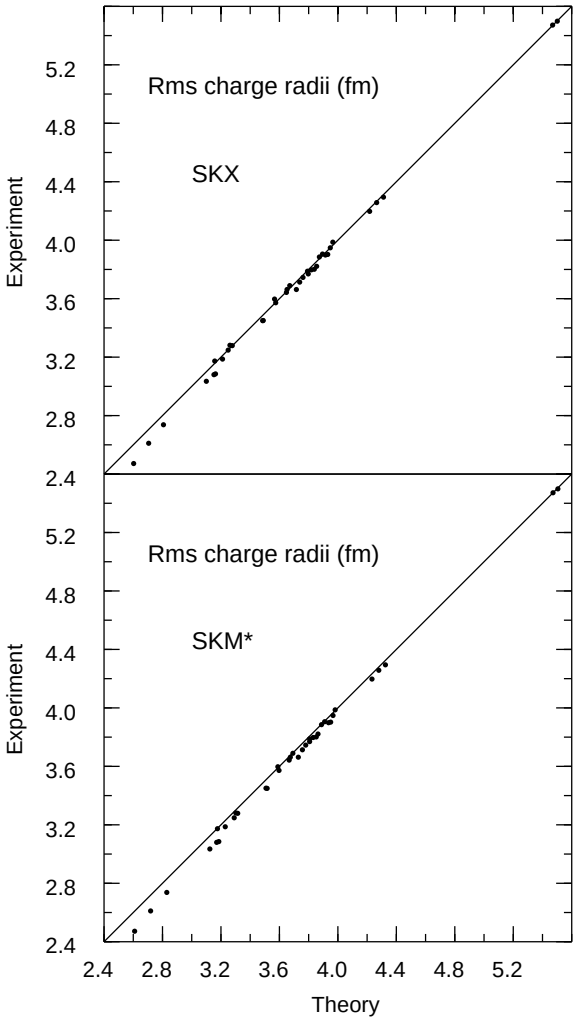

FIG. 1. Comparison of experimental and theoretical rms charge radii for the Skyrme interactions SKX (top panel) and SKM* (bottom panel).

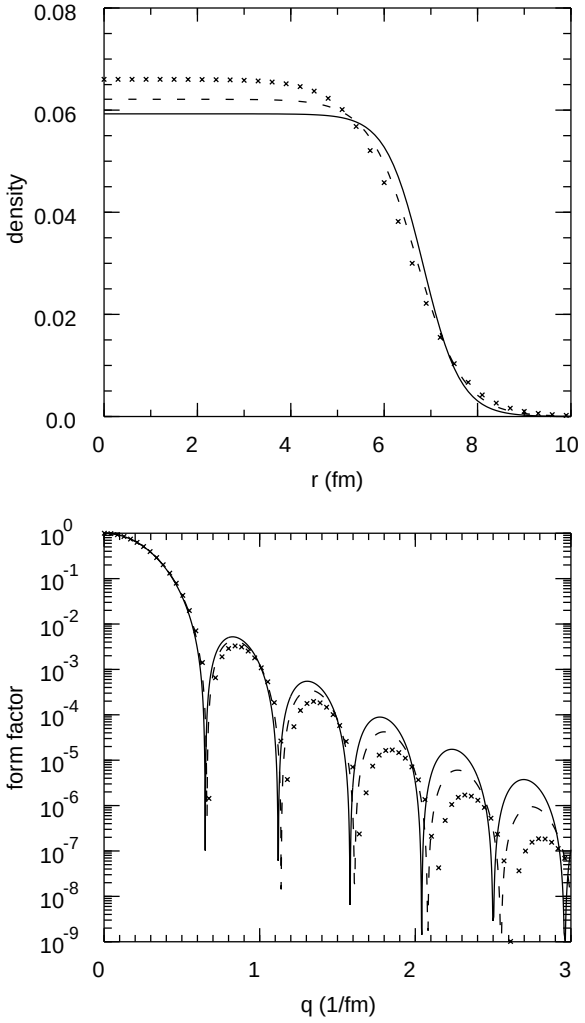

FIG. 2. Features of the Fermi-function densities and the associated form factors when the rms radius is constrained to be 5.5 fm. The results are given for diffuseness values $a=0.4$ fm (solid line), 0.5 fm (dashed line), and 0.6 fm (crosses).

increases toward the center of the distribution (where the number of protons is small). For example, for ^{92}Mo [16] the statistical and model-dependent error is 1.5% at $r=2$ fm, and goes down to 0.6% (about the size of the circles used to represent the experimental data in the figures to be discussed below) for $r=4$ fm.

The experimental and theoretical rms charge radii are compared in Fig. 1. The experimental radii are from Refs. [1,2], with those with the smallest errors selected in the case of more than one data set. The error in the experimental data is typically smaller than the size of the data points. The Hartree-Fock results for the two interactions SKM* (bottom panel) and SKX (top panel) are obtained with the CM (fractional) occupations (those obtained with ESP occupations are essentially the same). The excellent overall agreement between experiment and theory is not surprising since these rms charge radii are used to constrain the values of the Skyrme parameters. The deviations increase for light nuclei, going up to 5% for ^{12}C. In general, one may expect the mean-field approximation to be less valid for light nuclei.

In order to obtain a qualitative understanding of how the charge densities and form factors depend upon the diffuseness of the charge density, we show in Fig. 2 some charge densities for ^{208}Pb ($Z=82$) based on a Fermi distribution:

$$\rho(r)_{ch}=\frac{\rho_o}{1+\exp[(r-R)/a]}. \tag{8}$$

The Hartree-Fock (HF) models we consider are constrained to give essentially the same rms charge radii as observed in experiment (5.50 fm for ^{208}Pb). Thus we show three curves for the density in the upper part of Fig. 2 corresponding to values of the diffuseness of $a=0.4$ (solid line), 0.5 (dashed line), and 0.6 (crosses), but with R and ρ_o chosen to give $Z=82$ and the rms of 5.50 fm. The associated form factors $|F(q)|^2$ are shown in the lower panel. We note that an increase in the diffuseness is associated with an increase in the interior density and a large decrease in the form factor maxima at large q values. The qualitative effects of oscillations in the densities on the form factors are discussed in Ref. [17].

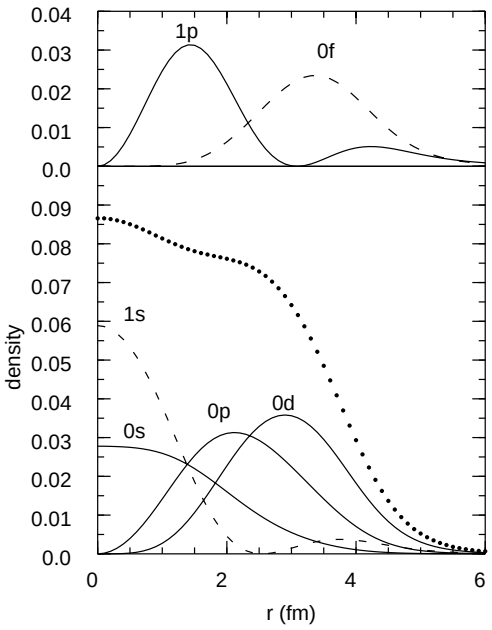

FIG. 3. The point-proton density (points) of ^{40}Ca in the SKX model with a closed-shell configuration. The total density is decomposed in terms of the contributions from the individual filled orbitals. In the upper panel the densities for protons in the orbitals just above the Fermi surface of ^{40}Ca are shown, for eight protons in the $0f_{7/2}$ orbit and for four protons in the $1p_{3/2}$ orbit.

In order to illustrate how the features of the charge density are built out of the specific shell-model orbitals which are filled, we show in Fig. 3 the point-proton density of ^{40}Ca (points) obtained with SKX with the assumption that the $0s$, $0p$, $1s$, and $0d$ orbits are filled. The individual contributions of the filled orbits to the proton density are shown. The $0s$ and $1s$ are the contributions from two protons in each of these orbits, respectively. The $0p$ indicates the sum of the four protons in the $0p_{3/2}$ orbit and two protons in the $0p_{1/2}$ orbit. The $0d$ indicates the sum of the six protons in the $0d_{5/2}$ orbit and four protons in the $0d_{3/2}$ orbit. In the top panel the densities associated with the (unfilled) valence orbits above the Fermi surface are shown; $0f$ for eight protons in the $0f_{7/2}$ orbit and $1p$ for four protons in the $1p_{3/2}$ orbit.

The features of the charge densities, which we will discuss below, can be understood on the basis of this type of microscopic decomposition of the total density in terms of the filled orbits. There is a direct connection when the protons are put into a specific orbit. For example, only the s orbits can contribute to the densities near the origin.

We will also discuss the isotopic change in the charge density when neutrons are added to specific orbitals. In this case the change in charge density is indirectly related to the orbits which are filled by neutrons since this will determine the change in the self-consistent HF potential. Thus the addition of neutrons will polarize the protons in a way which is dependent upon the density distribution of the orbits being occupied.

The change in the number of neutrons will change the proton potential in two ways. First, (a) there is the perturbative potential generated directly by the density change. For example, the density of the $0f$ orbit is surface peaked; hence the change in the proton potential generated by the addition of neutrons to the $0f$ orbit will pull out the core protons causing a drop in the interior charge density. In contrast, the $1p$ orbit has two peaks in the density, one in the nuclear interior and another at the surface. The proton potential generated from adding a neutron in the $1p$ orbit will have both interior and exterior contributions.

Second, (b) there is a self-consistent density saturation effect. When neutrons (or protons) are added into orbits with some interior density, the HF solution may require the entire nucleus to swell in order to reduce the overall interior density. This effect was recently discussed [18] in connection with an upward bend in the matter radii of neutron-rich sd-shell nuclei beyond $N=14$. The change in the proton potential due to addition of neutrons in a specific orbit will depend on a combination of these direct (a) and indirect (b) effects.

III. GENERAL FEATURES OF THE COMPARISON TO EXPERIMENT

For comparison between experiment and theory, we first consider the charge densities over a wide range of mass. The experimental data for a selected set of nuclei are shown in Figs. 4 and 5 by the filled circles, and in the case of a second data set, by squares. In particular, we take ^{28}Si from Ref. [19], ^{32}S from Ref. [20] (circles) and Ref. [21] (squares), ^{40}Ca and ^{48}Ca from Ref. [22], ^{50}Ti and ^{52}Cr from Ref. [23], ^{54}Fe from Ref. [24], ^{58}Ni from Refs. [25] (circles) and [24] (squares), ^{88}Sr from Ref. [26], ^{90}Zr from Ref. [27], ^{92}Mo from Ref. [16], ^{204}Hg from Ref. [28], and ^{208}Pb from Refs. [29] (circles) and [30] (squares).

In Fig. 4 we compare the experimental charge densities to our most complete theoretical results obtained from the HF method, with occupation numbers from the shell-model configuration mixing (CM) calculations discussed in the Introduction. The results with SKX (dashed lines) and SKM* (solid lines) are shown. Both SKX and SKM* nicely reproduce the nucleus-dependent oscillations. The Hamiltonian parameters are obtained from fits to the rms charge radii, binding energies, and excited state energies of these nuclei. Thus the good agreement between experiment and theory for the nucleus-dependent oscillations observed in Fig. 4 are not a result of a ''fit'' to these data, but arise naturally from the underlying shell structure.

The main difference between the SKX and SKM* results is that the interior density is about 5% higher with SKM* compared to SKX, with SKM* in best overall agreement with experiment. Close inspection of the curves in Fig. 4 in the region where the density falls off reveals a slightly larger surface diffuseness for SKM* compared to SKX (the dashed line for SKX is slightly steeper than the line for SKM* in the surface). The correlation between the increased interior height with the increased diffuseness (when the rms radius is the same) is consistent with what is expected from the Fermi model shown in Fig. 2. The change between SKX and SKM* corresponds to a $\Delta a = 0.036$ fm for ^{208}Pb. The change in the diffuseness is connected to the difference in the density-dependent part of the Hamiltonians, namely, $[\rho(r)]^{1/2}$ for

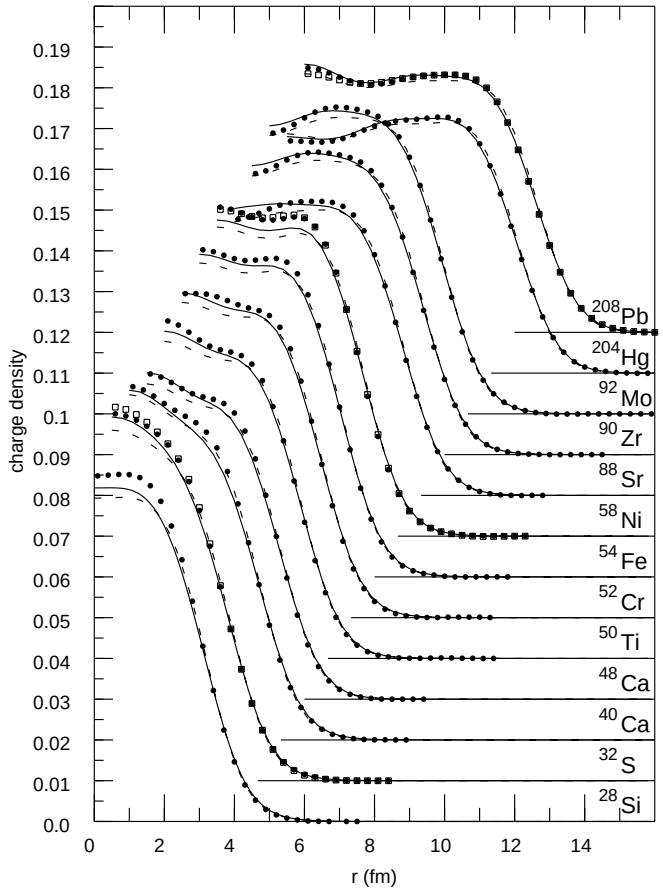

FIG. 4. Experimental charge-density distributions (filled circles) compared with the SKX (dashed lines) and SKM* (solid lines) calculations. In both cases the occupation numbers for the non-closed-shell nuclei are obtained from valence configuration mixing calculations. The charge-density units are in e fm^{-3}. Beyond ^{28}Si the curves and data have been progressively offset by 1 fm and 0.01 in the charge density. The data are discussed in the text.

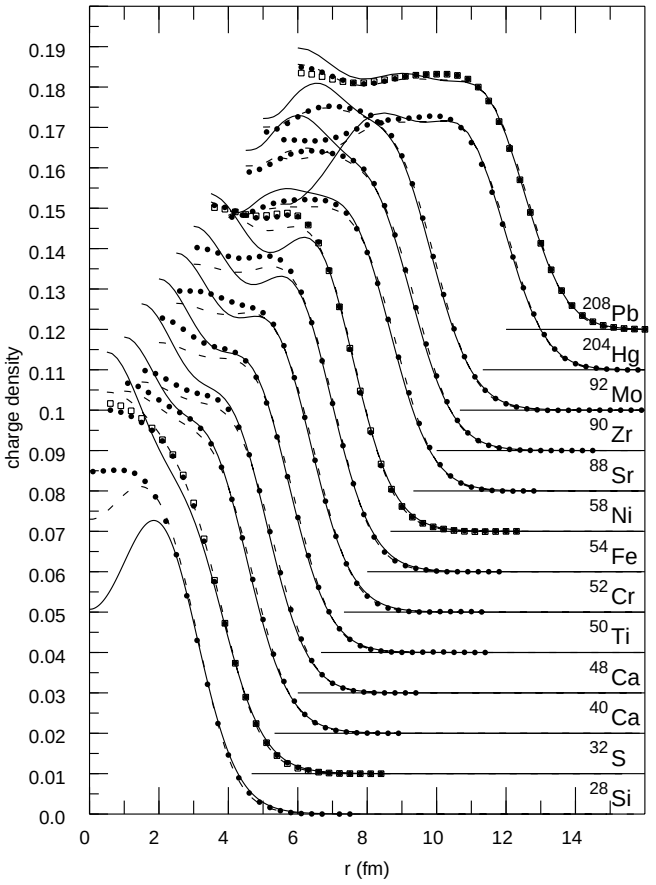

FIG. 5. Experimental charge-density distributions (filled circles) compared with the Woods-Saxon potential (solid lines) and SKX (dashed lines) calculations. In both cases ESP occupation numbers are used. A second data set is indicated by squares. The charge-density units are in e fm^{-3}. Beyond ^{28}Si, the curves and data have been progressively offset by 1 fm and 0.01 in the charge density. The data are discussed in the text.

SKX and $[\rho(r)]^{1/6}$ for SKM*. There is agreement between experiment and theory to an accuracy of about 2% or better for $r>1$ fm with SKM*. As discussed above, this is about the level of the accuracy with which these densities can be experimentally determined.

In this overview of Fig. 4 one can observe several interesting features associated with how the quantum waves change with shell structure and mass. Between ^{28}Si and ^{32}S in the sd shell there is a large increase in the interior density due to the filling of the $1s_{1/2}$ orbital (see also Ref. [21]). Likewise, between ^{204}Hg and ^{208}Pb there is a large increase in the interior related to the filling of the $2s_{1/2}$ orbital. Between ^{40}Ca and ^{48}Ca one observes a redistribution of the charge (proton) density due to the interaction with the valence $0f_{7/2}$ neutrons. The theoretical density distributions for the sequence ^{48}Ca, ^{50}Ti, ^{52}Cr, and ^{54}Fe show a smoothly varying trend due to dominance of the proton $0f_{7/2}$ subshell filling. The fine details of the interior oscillations in experiment are not as smooth as those calculated; however, this may be due to the error in the Fourier-Bessel analysis.

In Fig. 5 the charge densities obtained with some approximations to the full calculations are shown. The dashed line shows the results obtained with the SKX HF method with ESP occupation numbers. Comparison of the dashed lines in Fig. 4 (SKX with CM occupations) and Fig. 5 (SKX with ESP occupations) shows that the more exact CM calculations usually lead to better agreement with the data.

The solid line in Fig. 5 shows densities obtained from a typical Woods-Saxon (non-self-consistent) potential [31] and with ESP occupation numbers. Comparison of the dashed and solid lines in Fig. 5 shows that the Woods-Saxon potential produces density oscillations which are too large compared to experiment. The density oscillations are sensitive to the oscillations in the potential. In heavy nuclei such as ^{208}Pb, the HF proton potential is dominated by contributions from the neutron density. Since the proton and neutron densities are out of phase, the proton and neutron density oscillations tend to become dampened in self-consistent calculations compared to those obtained from the flat Woods-Saxon potential.

A comparison between the calculated and experimental charge-density distributions should not be considered independently of the electron scattering form factors, as the latter are the basic quantities measured experimentally. Thus we

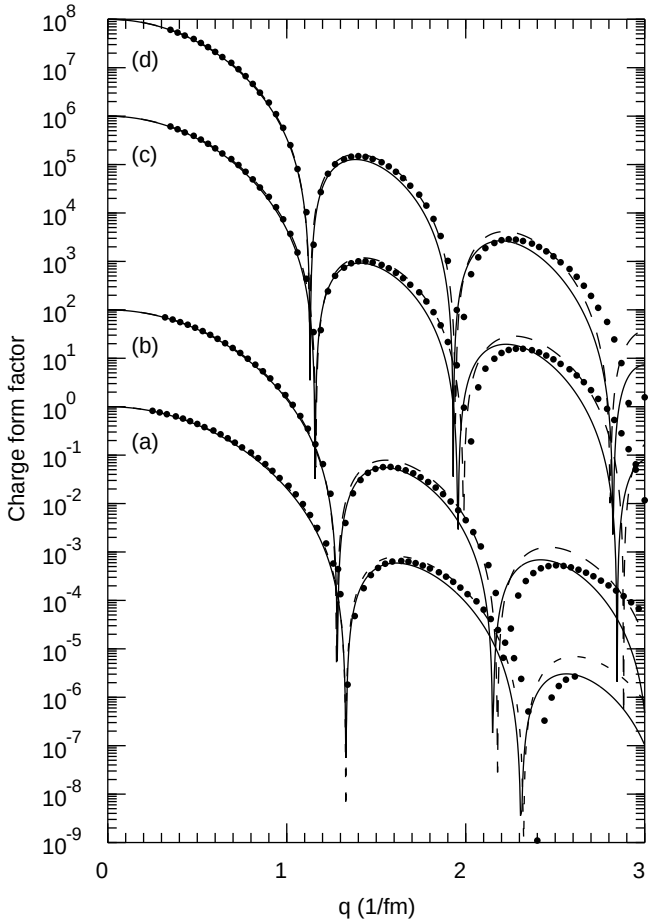

FIG. 6. Longitudinal elastic electron scattering form factors versus momentum transfer q (fm^{-1}) for ^{28}Si (a), ^{32}S ($\times 10^2$) (b), ^{40}Ca ($\times 10^6$) (c), and ^{48}Ca ($\times 10^8$) (d). The filled circles represent the experimental data over the observed range of momentum transfer. The theory is SKX (dashed line) and SKM* (solid line). The occupation numbers are taken from shell-model configuration mixing.

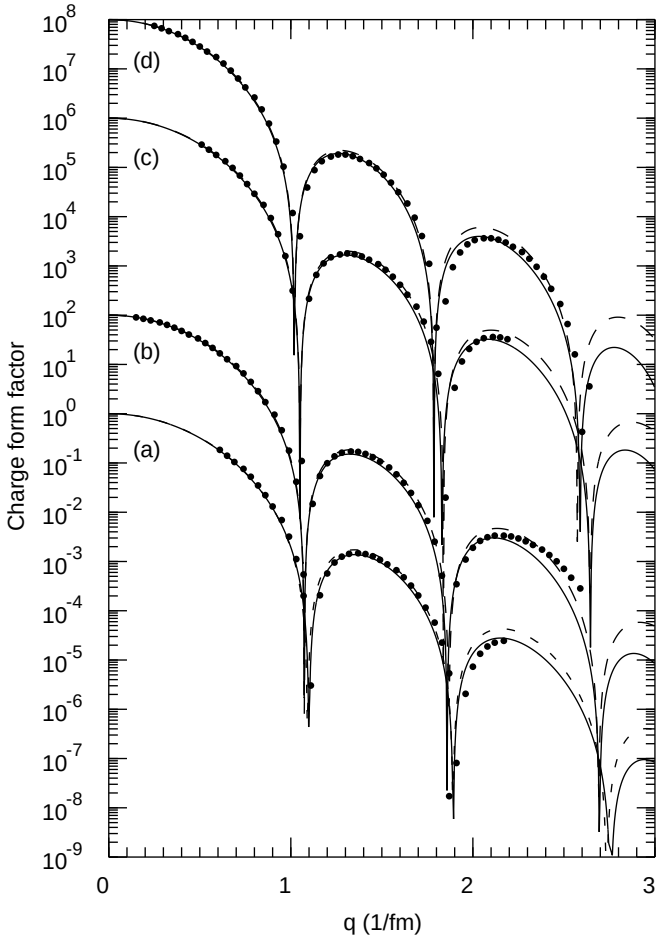

FIG. 7. Longitudinal elastic electron scattering form factors versus momentum transfer q (fm^{-1}) for ^{50}Ti (a), ^{52}Cr ($\times 10^2$) (b), ^{54}Fe ($\times 10^6$) (c), and ^{58}Ni ($\times 10^8$) (d). See caption to Fig. 6.

show in Fig. 6 ($A=28$–48), Fig. 7 ($A=50$–58), Fig. 8 ($A=88$–92), and Fig. 9 ($A=204$–208) the plane-wave form factors $|F(q)|^2$ associated with the densities in Figs. 4 and 5. The circles for the experimental data are given only over the range of momentum transfers measured experimentally. The form factors are compared with the calculated SKX and SKM* results. Agreement between experiment and theory is excellent out to about 2.5 fm^{-1}, and then quickly becomes worse at higher momentum transfer. The main difference between the SKX and SKM* form factors is that SKM* falls off a little faster and is generally in better agreement with the experiment at a higher momentum transfer. This faster falloff can be associated with the increase in the surface diffuseness discussed above in connection with Fig. 2.

Disagreement between experiment and theory above 2.5 fm^{-1} (and the associated discrepancies in the charge densities) might be related to two factors. First, the Skyrme interaction is a low-momentum expansion of the effective interaction, and one must expect the density fluctuations resulting from this approximation to break down at some point. Second, mesonic-exchange corrections to the charge form factor become increasingly important at higher momentum transfers [32].

IV. EXTENDED RESULTS FOR SPECIFIC MASS REGIONS

We next extend the preceding results for the Skyrme Hartree-Fock calculations with a view to making more extensive comparisons with the available electron scattering data for p-shell, sd-shell, pf-shell, and Pb-region nuclei. For these comparisons we use the SKM* Skyrme interaction with ESP orbital occupations and with the occupations obtained from the CM calculations discussed in the Introduction. The experimental data shown in the figures are from the Fourier-Bessel decomposition given in Table IX of Ref. [1].

A. p-shell charge-density distributions

The results of the comparisons between experiment and our calculations with the SKM* interaction are given in Fig. 10. The calculations based on the ESP are indicated with a dashed line, and those using CM occupancies based on the shell model with solid lines. For ^{12}C the CM occupancies are obtained from the the PJT Hamiltonian [4] in the

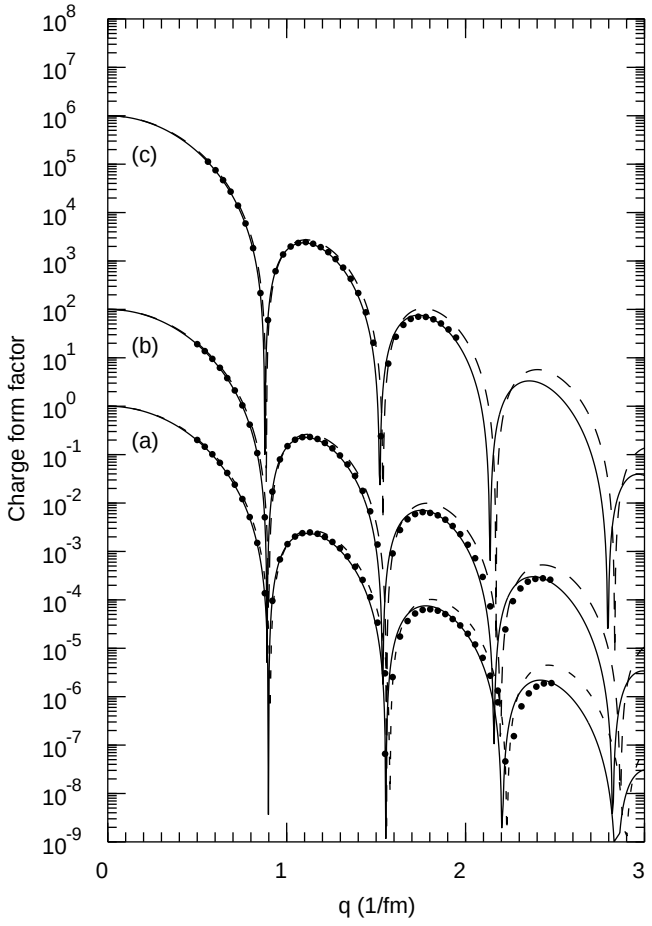

FIG. 8. Longitudinal elastic electron scattering form factors versus momentum transfer q (fm^{-1}) for ^{88}Sr (a), ^{90}Zr ($\times 10^2$) (b), and ^{92}Mo ($\times 10^6$) (c). See caption to Fig. 6.

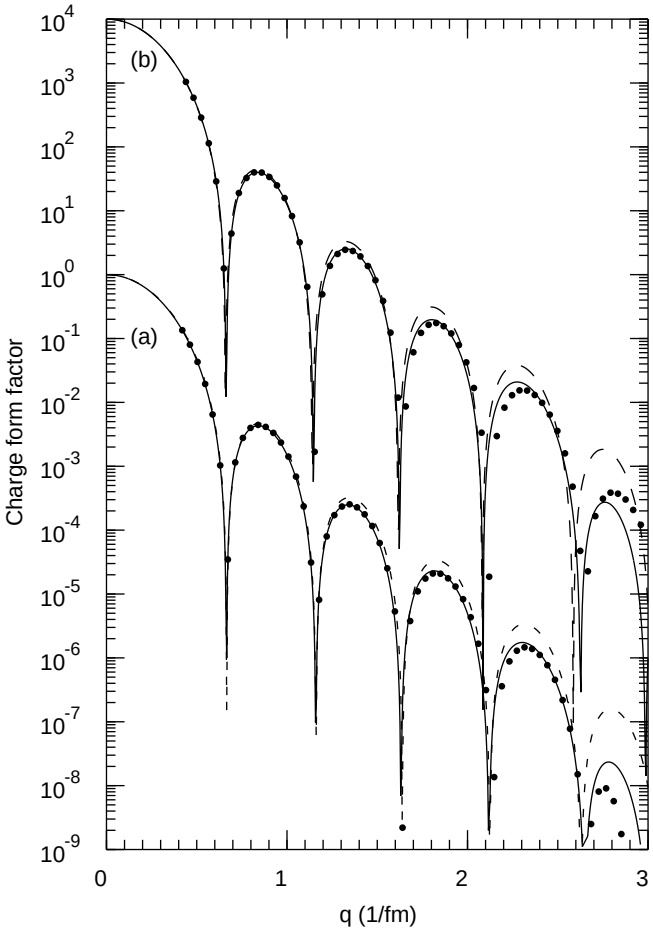

FIG. 9. Longitudinal elastic electron scattering form factors versus momentum transfer q (fm^{-1}) for ^{204}Hg (a) and ^{208}Pb ($\times 10^4$) (b). See caption to Fig. 6.

$(0p_{3/2},0p_{1/2})$ model space. ^{16}O is treated as closed shell, and ^{15}N is treated as a closed shell plus one hole in the $0p_{1/2}$ orbit. In general, it is found that the Skyrme Hartree-Fock calculations give a good reproduction of the density distributions in the tail region, whereas in the interior region there are more marked differences between theory and experiment. The deviations from experiment in the interior region are fairly large for these light nuclei, where the mean-field approximation is expected to have less validity. The use of shell-model occupation numbers leads to some improvement in the agreement only for ^{12}C. The difference between ESP and shell-model occupations for ^{12}C is due to the difference in the $0p_{3/2}$ and $0p_{1/2}$ single-particle proton densities generated by the spin-orbit part of the Skyrme potential.

B. *sd*-shell charge densities

The data includes all of the charge-density distributions given in Refs. [1] and [2] for *sd*-shell nuclei. The results of the comparisons are shown in Figs. 11, 12, and 13. Generally isotopes of a particular element have been grouped in a single figure. The CM occupancies were obtained with the USD Hamiltonian [5] in the $(0d_{5/2},0d_{3/2},1s_{1/2})$ model space.

Reasonable agreement is found between experiment and theory for the SKM* interaction using the ESP occupancies. Employing shell-model occupancies from configuration mixing leads to consistently better agreement, generally within about 4%. The calculated densities tend to be slightly less than the experimental densities in the interior region in most cases.

Some interesting physical effects due to the configuration mixing can be noted, for example, for the Si (Fig. 11) and S isotopes (Fig. 13). The number of nodes in the proton single-particle radial wave functions (or equivalently, the number of peaks in the corresponding probability density distribution) determine the shape of the overall charge-density distribution. For ^{28}Si there is no proton occupation of the $1s_{1/2}$ orbital in the ESP model. As a consequence, the calculated interior density (dashed line) for small radii in ^{28}Si is substantially lower than the experimental density. The effect of configuration mixing (solid line) is to introduce protons into the $1s_{1/2}$ subshell, and the interior-peaked form of the associated probability density increases the interior density to give better agreement with experiment. For ^{29}Si and ^{30}Si the additional neutrons have a polarizing effect on the core, which progressively pulls out the protons to lower the interior density—this effect can clearly be seen both in the experimental and theoretical curves.

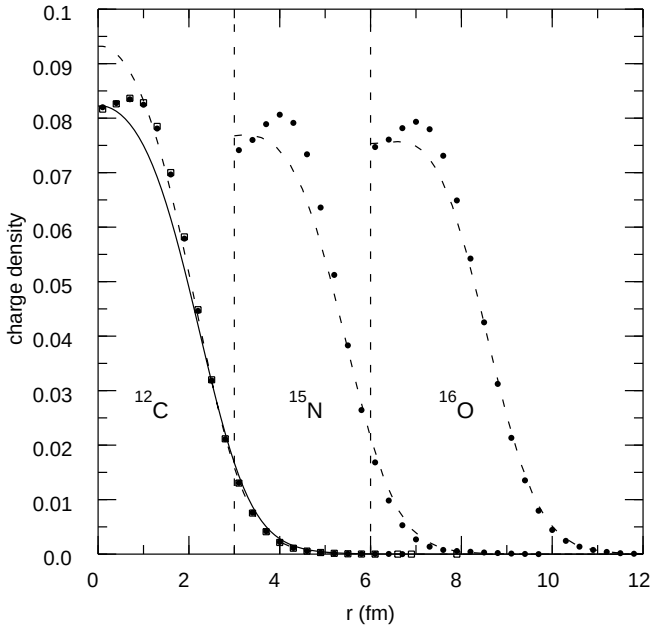

FIG. 10. The experimental charge-density distributions for the nuclei ^{12}C, ^{15}N, and ^{16}O are given by the filled circles and compared with the calculated SKM* distributions which have ESP occupancies (dashed lines), and those which include configuration mixing (solid lines). A second data set is indicated by squares. The charge densities are in units of e fm^{-3}.

For ^{32}S the $1s_{1/2}$ subshell is completely filled in the ESP model, which results in a theoretical interior density (dashed line) for small radii (which is higher than experiment). Including configuration mixing (solid line) shifts protons out of the $1s_{1/2}$ subshell, thereby lowering the interior density to give improved agreement with experiment. The same polarizing effect of the extra neutrons in the other two sulfur isotopes is also evident in Fig. 13.

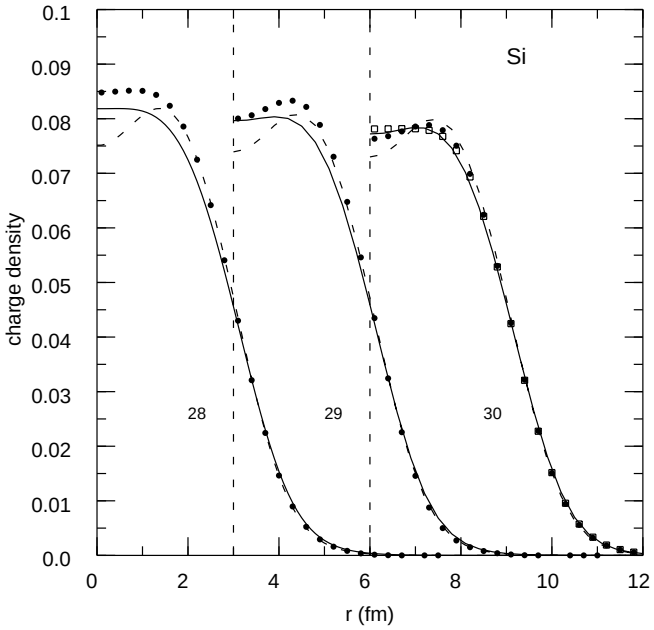

FIG. 11. Comparison for Si isotopes with $A=28$, 29, and 30. The same convention is followed as for Fig. 10.

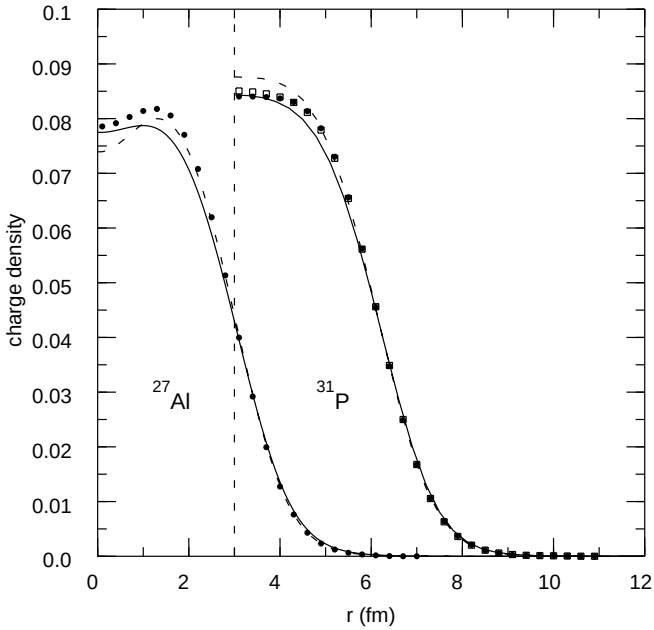

FIG. 12. Comparison for the nuclei ^{27}Al and ^{31}P. The same convention is followed as for Fig. 10.

C. *pf*-shell charge densities

In this section we discuss the charge densities for 20 pf-shell nuclei from $A=40$–70. ^{40}Ca is treated as a closed shell. The CM occupation numbers for the nuclei ($A=48$–65) are obtained with the FPD6 pf-shell Hamiltonian [6] in the $(0f_{7/2},0f_{5/2},1p_{3/2},1p_{1/2})$ model space.

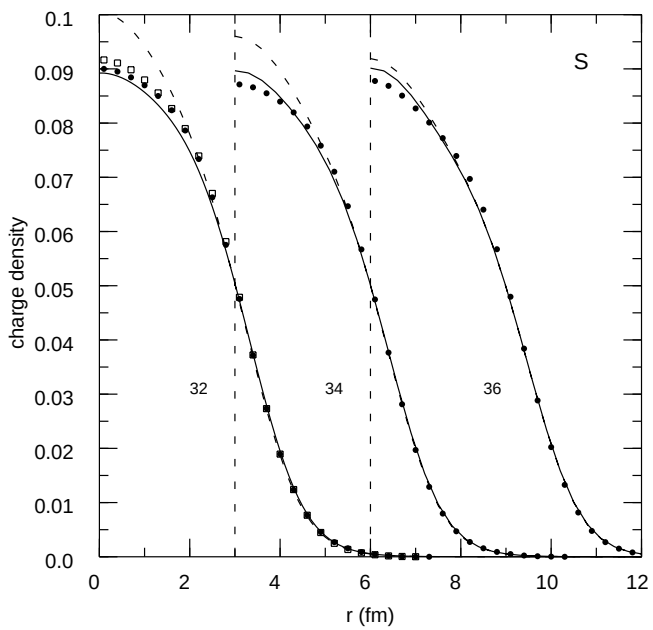

FIG. 13. Comparison for the S isotopes with $A=32$, 34, and 36. The same convention is followed as for Fig. 10.

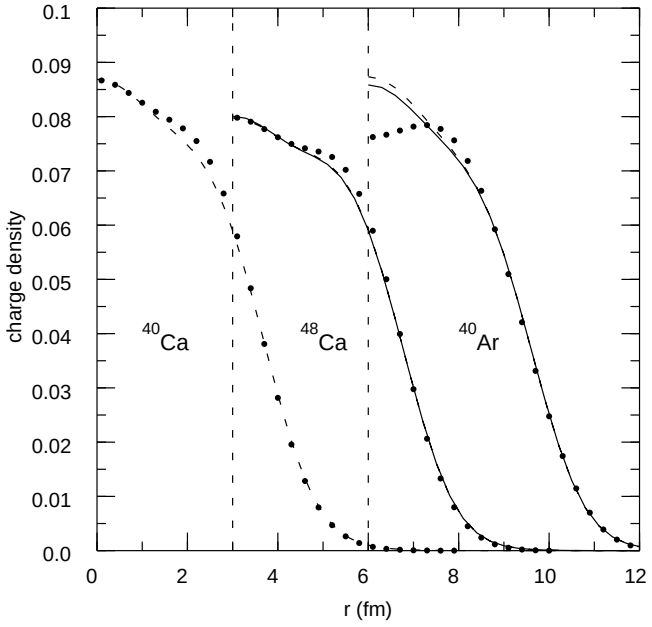

FIG. 14. Charge densities for ^{40}Ca, ^{48}Ca, and ^{40}Ar. The same convention is followed as for Fig. 10.

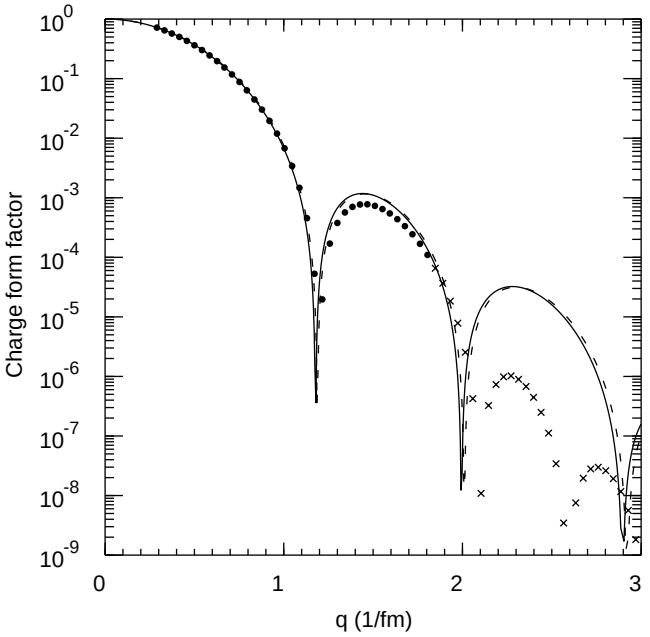

FIG. 15. Form factor for ^{40}Ar.

Perhaps the best example of the polarizing effect of valence neutrons on the core protons is observed for ^{40}Ca and ^{48}Ca in Fig. 14, where for the latter the eight neutrons in the $0f_{7/2}$ subshell in the ESP model lead to a substantial lowering of the charge-density distribution relative to ^{40}Ca.

We also include the density for ^{40}Ar in Fig. 14, which has two proton holes in the sd shell and two neutron particles in the pf shell. The agreement between experiment and theory for the interior region appears to be significantly worse compared to ^{40}Ca or ^{36}S (Fig. 13). However, this is probably due to a particularly large uncertainty in the Fourier-Bessel fit which is obtained from data only up to $q_{max}=1.8$ (1/fm). The form factor data up to q_{max} are shown by the filled circles in Fig. 15. The crosses beyond this point show how the Fourier-Bessel fit extrapolates to higher q. The extrapolation is clearly unrealistic when compared with other data in this mass region (see Fig. 6), which are measured up to a higher q_{max} value.

For the Ti isotopes in Fig. 16 the addition of two extra neutrons to ^{48}Ti also lowers the theoretical interior charge density. The rise in the ^{50}Ti interior density for $r<1$ fm may be an error resulting from the lack of data above $q=2.2$ fm^{-1} (see Fig. 7). A similar effect is observed for the difference between the ^{52}Cr and ^{50}Cr charge densities when two neutrons are added to the $0f_{7/2}$ orbit. Due to the $0f_{7/2}$ subshell closure at ^{48}Ca and ^{56}Ni, the occupations obtained in the pf-shell configuration mixing are still dominated by the addition of protons and neutrons to the $0f_{7/2}$ shell, and there is not much difference between the ESP (dashed line) and configuration mixing (solid lines) models for these nuclei in Figs. 14, 16, and 17, with N and Z between 20 and 28.

In the ESP model, ^{54}Cr differs from ^{52}Cr by the addition of two neutrons in the $1p_{3/2}$ orbital. The density of the $1p_{3/2}$ orbit has both a surface and an interior part. In Fig. 18 we show the difference between the proton potentials of ^{54}Cr and ^{52}Cr when two neutrons are added to the $1p_{3/2}$ orbit (the dashed line). As discussed in Sec. II, this change in the neutron potential results from a combination of (a) a perturbative change in the proton potential due to the two neutrons added in the $1p_{3/2}$ and (b) a nonperturbative change due nuclear saturation. The result is that there are two regions where the potential increases, with a net effect that at least some protons are pulled in, thereby creating an increase in the ^{54}Cr interior charge density compared to that of ^{52}Cr (the dashed lines in Fig. 17). If the two neutrons are added to the $0f_{5/2}$ orbit, the potential only increases at the nuclear surface (the

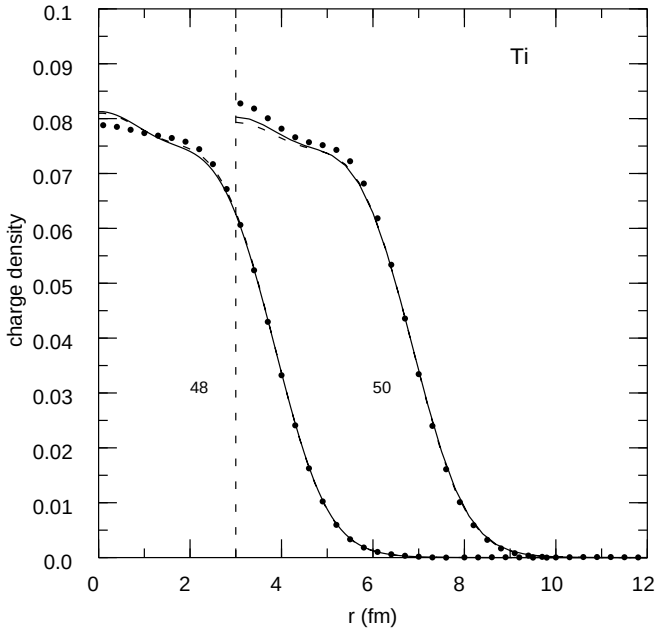

FIG. 16. Comparison for the Ti isotopes with $A=48$ and 50. The same convention is followed as for Fig. 10.

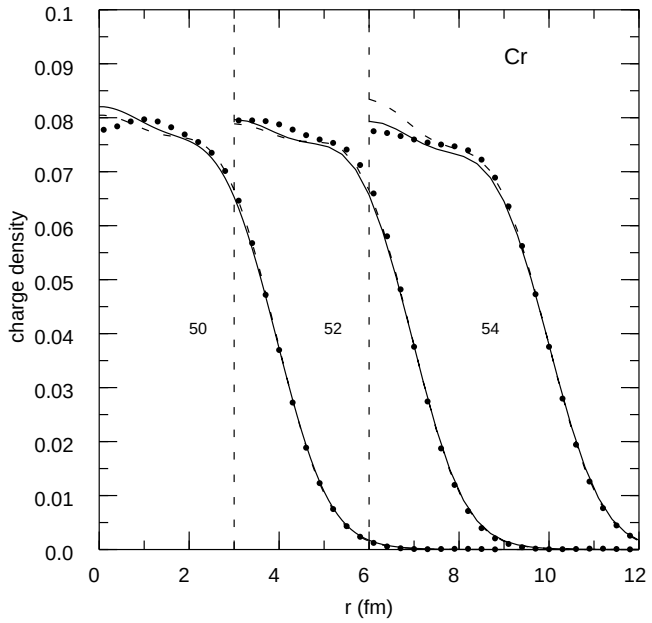

FIG. 17. Comparison for the Cr isotopes with $A=50$, 52, and 54. The same convention is followed as for Fig. 10.

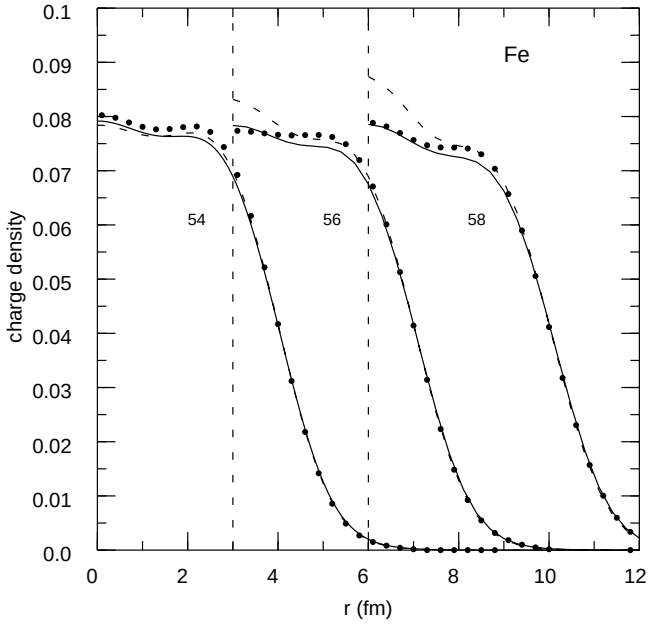

FIG. 19. Comparison for the Fe isotopes with $A=54$, 56, and 58. The same convention is followed as for Fig. 10.

line in Fig. 18) and the protons are pulled out, similar to the situation discussed above in connection with the $0f_{7/2}$ neutron orbit in ^{52}Cr-^{50}Cr. The configuration mixing in ^{54}Cr distributes the two neutrons about equally between the $1p_{3/2}$ and $0f_{5/2}$ orbitals, with the result that the CM charge densities for ^{54}Cr and ^{52}Cr (the solid lines in Fig. 17) are very similar.

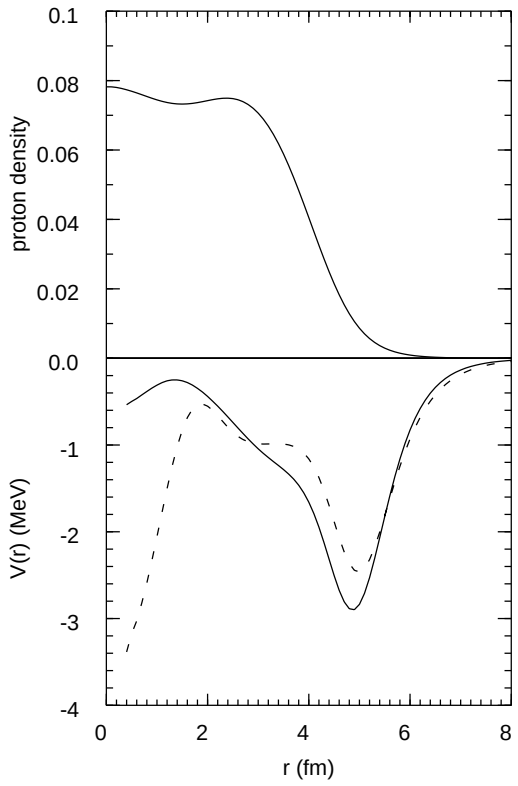

FIG. 18. The bottom panel shows the change in the proton potential between ^{54}Cr and ^{52}Cr when the two neutrons are added to the $1p_{3/2}$ orbit (dashed line) or to the $0f_{5/2}$ orbit (solid line). The top panel shows the point-proton density for ^{52}Cr.

A similar result is found for the Fe isotopes in Fig. 19. In the ESP model the neutrons are added to the $1p_{1/2}$ orbit and the protons are pulled in, resulting in an increase in the interior density (dashed line). With configuration mixing the valence neutrons are divided about equally between the $1p_{3/2}$ and $0f_{5/2}$ orbits, and there is little change in the charge density (solid lines) among the various isotopes. The most systematic deviation between experiment and theory in the lower-to-mid pf-shell region is that experiment is up to about 5% higher than theory in the shoulder region of the density.

The general reduction in the interior charge density with the addition of neutrons can also be seen for the Ni isotopes (Fig. 20) and Cu isotopes (Fig. 21). The effect of configuration mixing on the interior charge density is also evident for ^{59}Co in Fig. 21. At this higher end of the pf shell, the charge densities obtained with configuration mixing are generally in better agreement with experiment than those of the ESP model. However, the calculated values (solid lines) tend to be systematically less than experiment. The extrapolation implied for the FPD6 interaction [6], which is based on experimental energy data in the $A=41-49$ mass region, is considerable. It will be interesting to use the new ''universal'' pf-shell interactions obtained in Ref. [33] to calculate the charge densities in the upper part of the shell. In addition, the $0g_{9/2}$ orbital will become more important.

In summary, good agreement between experiment and theory is obtained for most of the pf-shell nuclei, with deviations within about 2–3 %, except towards the upper end of the shell where larger deviations are evident. In general, the use of shell-model occupation numbers leads to improved agreement, in some cases significantly so.

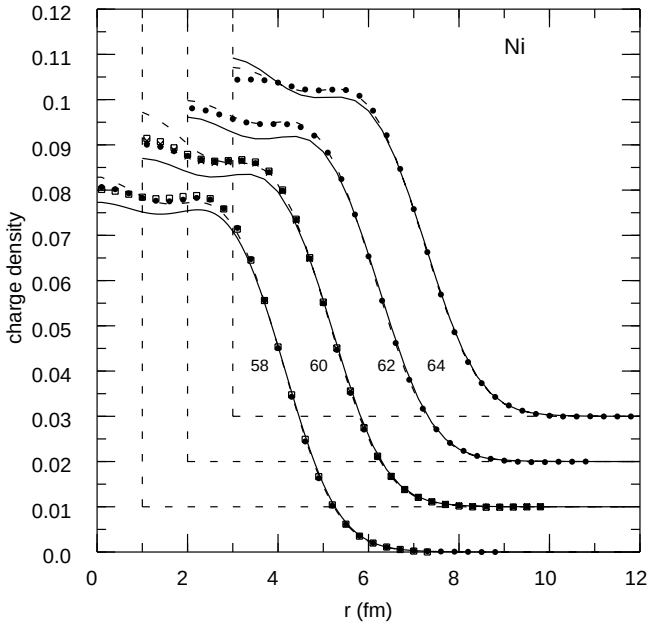

FIG. 20. Comparison for the Ni isotopes with $A=58$, 60, 62, and 64. The same convention is followed as for Fig. 10.

D. Pb-region nuclei

The experimental charge densities for ^{204}Hg and ^{208}Pb are shown Fig. 4. Our SKM* results for ^{208}Pb are the same as those of Ref. [34]. One observes good agreement for all radii including the region near the origin which is sensitive to the occupancy of the $2s_{1/2}$ proton orbital. In contrast, in the relativistic Hartree model for ^{208}Pb, one finds that the interior density is reduced compared to theory, leading to the conclusion that the $2s_{1/2}$ proton orbit is depleted [35]. (In Ref. [35] and many other references, this *s* state is called the $3s$ orbit

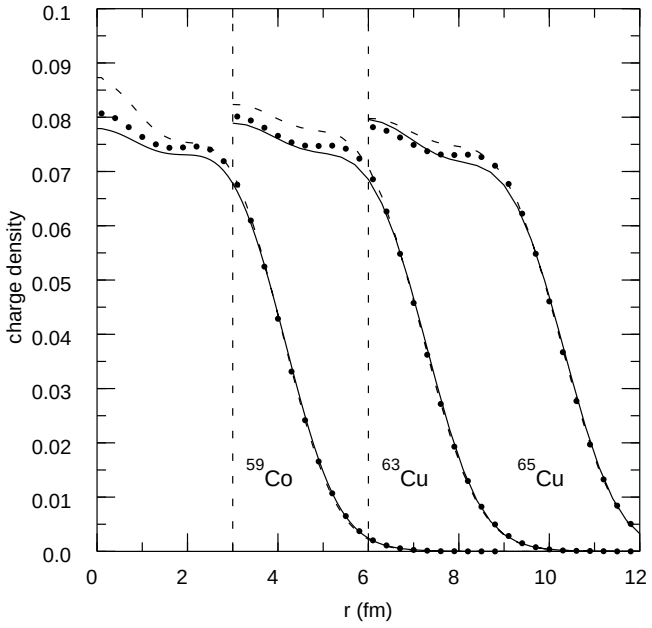

FIG. 21. Comparison for the nuclei ^{59}Co, ^{63}Cu, and ^{65}Cu. The same convention is followed as for Fig. 10.

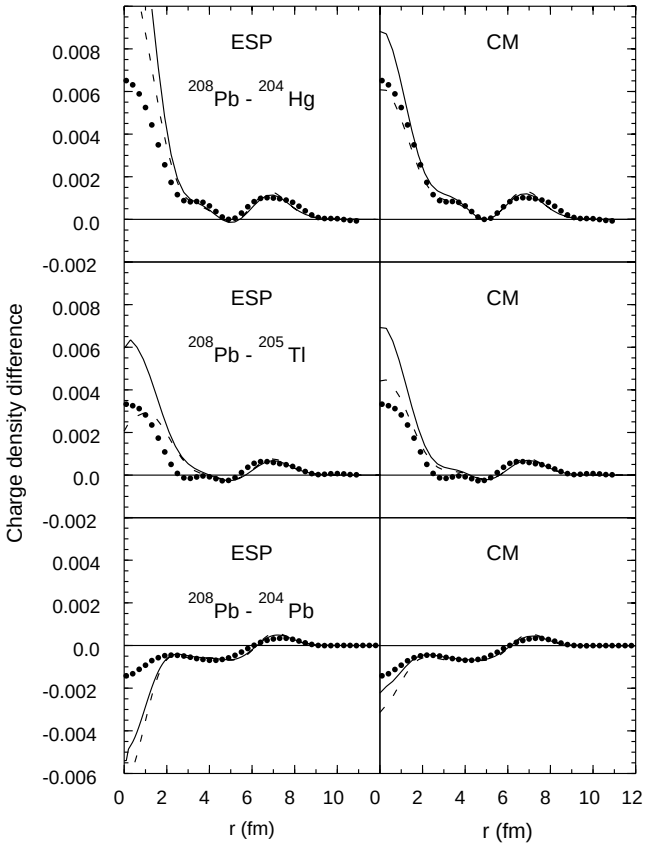

FIG. 22. Charge-density differences $\Delta\rho(r)_{ch}$ for ^{204}Pb, ^{205}Tl, and ^{204}Hg relative to ^{208}Pb. The experimental data (filled circles) are compared with the SKX (solid lines) and SKM* (dashed lines) HF models. The HF calculations were carried out with orbit occupancies from ESP and CM models.

since the counting of the radial quantum number starts from one rather than our convention of starting at zero.) We remarked in Sec. II that the dramatic change in the interior density between ^{208}Pb and ^{204}Hg was related to the fact that in the ESP model these nuclei differ by two protons in the $2s_{1/2}$ orbital. (In the ESP model they also differ by the two neutrons in the $2p_{1/2}$ orbital, whose effect will be discussed below.)

To go beyond the previous works, we consider the charge-density differences of ^{208}Pb, ^{206}Pb, ^{206}Tl, and ^{204}Hg in a model beyond the ESP model. For CM, in these nuclei we assume that ^{208}Pb is a closed shell, and that neutron holes go into the $(0h_{9/2},1f_{7/2},1f_{5/2},2p_{3/2},2p_{1/2},0i_{13/2})$ orbits and proton holes go into the $(0g_{7/2},1d_{5/2},1d_{3/2},2s_{1/2},0h_{11/2})$ orbits. In this model space we use the Kuo-Herrling interaction [8].

This orbital at the Fermi surface of ^{208}Pb is also involved in the ^{208}Pb$(e,e'p)^{207}$Tl experiment [12] where the data requires a spectroscopic factor of $S=1.2$ compared to the expectation in the ESP model of $S=2$. Thus there has been much interest in understanding how this reduction of the spectroscopic factor affects the charge densities of the Pb, Tl, and Hg isotopes.

We show in Fig. 22 the difference in the charge densities of ^{204}Pb, ^{204}Hg, and ^{205}Tl with that of ^{208}Pb. The data are

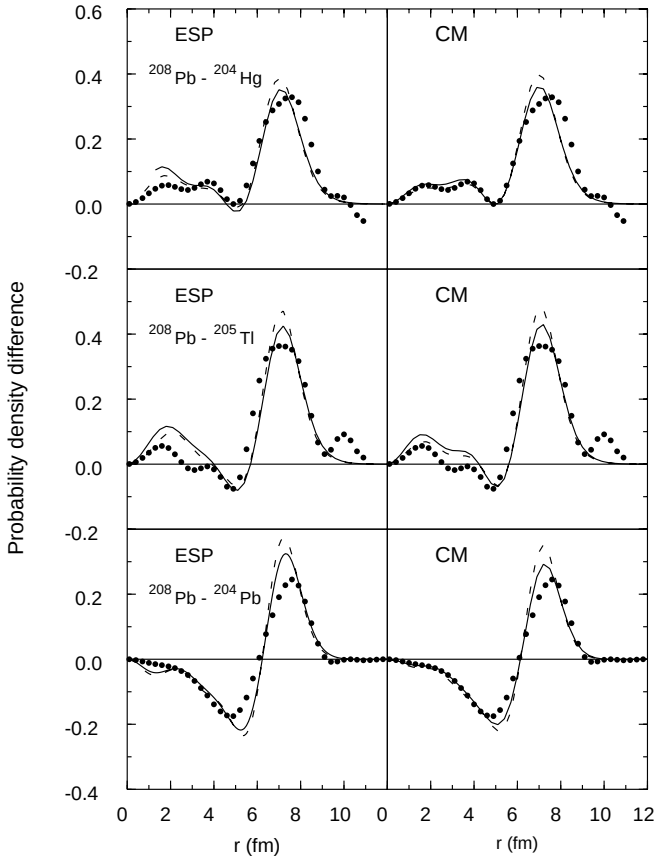

FIG. 23. Charge probability density differences $4\pi r^2 \Delta\rho(r)_{ch}$. See caption to Fig. 22. The probability density difference for ^{208}Pb-^{204}Hg has been divided by 2.

taken from Fourier-Bessel fits of Ref. [1]. The corresponding differences in the charge probability densities $P(r)$ [Eq. (3)] are shown in Fig. 23. One observes in Fig. 23 some oscillations in the experimental charge probability densities beyond $r=10$ fm, which must be an artifact of the truncation in the Fourier-Bessel representation of the experimental form factors. In the Fourier-Bessel analysis of ^{206}Pb given in Refs. [1,2], these spurious oscillations are much larger. In the HF calculations the ^{204}Pb-^{208}Pb difference is to a good approximation just two times that of ^{206}Pb-^{208}Pb. Thus the conclusions we draw from a comparison to the better ''data'' for ^{204}Pb should also apply to ^{206}Pb.

The experimental densities are compared with those calculated with the SKX and SKM* HF models with orbit occupations from the ESP and CM models. In the ESP model the ^{205}Tl and ^{204}Hg differences arise from the addition of one and two protons in the $2s_{1/2}$ orbital, respectively. The main contribution to the difference is due to the density of the $2s_{1/2}$ proton orbit, but there are also contributions coming from the polarization of the core protons due to the addition of protons and neutrons. The effect of polarization is illustrated by the ^{208}Pb-^{204}Pb density difference shown at the bottom of Figs. 22 and 23. Configuration mixing of the valence neutrons is important for the interior part of the density difference, with the CM model in better with experiment compared to the ESP model. Theoretically, the contribution from the polarization of the two neutrons in the ^{204}Hg-^{208}Pb and ^{205}Tl-^{208}Pb charge-density differences is given to a good approximation by one-half of the ^{204}Pb-^{208}Pb charge-density difference.

For ^{205}Tl the one-proton hole (relative to a closed shell for ^{208}Pb) is spread in the CM model over the $2s_{1/2}$ (0.89) and the $1d_{5/2}$ and $1d_{3/2}$ (0.11) orbits (the number in brackets is the difference in the orbit occupations between ^{205}Tl and ^{208}Pb). For ^{204}Hg the two-proton holes are spread in the CM model over the $2s_{1/2}$ (0.95), the $1d_{5/2}$ and $1d_{3/2}$ (0.87), and the $0g_{7/2}$ (0.04) and the $0h_{11/2}$ (0.14) orbits. The agreement between experiment and theory is good especially when configuration mixing is taken into account. The probability densities in Fig. 23 show that the protons at the Fermi surface are most likely to be found at the surface of the nucleus. Again, agreement with experiment is excellent especially when configuration mixing is included.

The $(d,{}^3\mathrm{He})$ proton pickup and $(e,e'p)$ proton knock-out experiments also provide information on the orbit occupancies. These experiments are sensitive to the proton orbital densities near the nuclear surface (see Fig. 1 of Ref. [36]). When the results of these experiments are combined with an optical model analysis of the reaction, one can extract spectroscopic factors for proton removal to individual final states as well as for the sum over all low-lying final states.

With configuration mixing, our results for the proton removal spectroscopic factors are $S=2$ for ^{208}Pb$(e,e'p)^{207}$Tl (g.s.) (the ^{207}Tl ground state is one hole in the $2s_{1/2}$ orbital), and $S=1.56$ for ^{206}Pb$(e,e'p)^{205}$Tl (g.s.). The spectroscopic factors summed over all final states of a given j value give the orbit occupancy. For the $2s_{1/2}$ orbit this is $N_p=2$ for both ^{208}Pb and ^{206}Pb.

The spectroscopic factor obtained from a nonrelativistic optical potential analysis of the ^{208}Pb$(e,e'p)$ data [37] is $S=0.98(9)$, about a factor of 2 smaller than expected. The results of $S=1.40(8)$ obtained from a relativistic analysis of $(e,e'p)$ data [38] and $S=1.5$ from a new analysis of $(d,{}^3\mathrm{He})$ data [37] are in better agreement but still smaller than theory. [The original analysis of the $(d,{}^3\mathrm{He})$ data gave $S=1.8$.] The ratio of the $(e,e'p)$ spectroscopic factors to the ^{207}Tl and ^{205}Tl ground states of 0.69(3) [39] is a little smaller than the theoretical value of 0.78 [see Ref. [39] for a discussion of the ratio obtained with $(d,{}^3\mathrm{He})$]. Analysis of $(d,{}^3\mathrm{He})$ data on ^{208}Pb, ^{206}Pb, ^{205}Tl, and ^{204}Hg for the sum over low-lying $\ell=0$ states [40] gives $2s_{1/2}$ occupancies of 1.54(17), 1.35(17), 0.71(16), and 0.60(23), respectively, as compared to our CM values of 2.0, 2.0, 1.21, and 1.05, respectively. The changes in occupancy relevant for the ^{208}Pb-^{205}Tl and ^{208}Pb-^{204}Tl density differences are 0.83(24) and 0.94(29), respectively, from experiment compared to 0.79 and 0.95, respectively, from theory.

A remaining question is how to reconcile the good agreement between experiment and theory for the charge densities with the apparent depletion in the orbit occupancy obtained from an analysis of proton removal reactions. The charge-density differences discussed above by definition integrate to $Z_i - Z_f$ protons. When ^{208}Pb is treated as a closed shell, these $Z_i - Z_f$ protons come from the orbits just below the Fermi

surface as discussed above. Agreement with the charge densities suggests that one can find an effective mean-field potential, such as those obtained from SKX and SKM*, from which one can calculate effective single-particle densities that implicitly depend on the correlations via the effective mean field. This idea is discussed in terms of the quasihole orbits by Pandharipande *et al.* [36]; note in particular the similarity of quasihole density for the $2s$ orbital for a liquid drop of 70 ^{3}He atoms with those shown in Fig. 23.

V. CONCLUSIONS

It has been shown that nuclear radii extracted from electron scattering experiments agree well with those calculated from the spherical Skyrme Hartree-Fock approach. Good general agreement has also been found in extensive comparisons of measured nuclear charge-density distributions with calculated values for p-shell, sd-shell, and pf-shell nuclei and some selected magic and semimagic nuclei up to Pb, using the SKM* and SKX Skyrme interactions. The extent of the agreement is, in most cases, significantly further improved by constraining the Hartree-Fock calculations to use shell-model occupancies. Somewhat larger deviations are observed for lighter nuclei, which probably relate to the adequacy of the mean-field approximation for these nuclei.

We have discussed the comparison between experiment and theory both in terms of the form factors, where the data are precise over the range of momentum measured, and in terms of the more physically intuitive charge densities. We have shown several examples where unphysical rapid oscillations may occur in the experimental densities. These are conventionally treated as part of the ''error band'' in the Fourier-Bessel fits. However, it might be useful to introduce some reasonable model dependence in the extraction of charge densities in order to eliminate unphysically rapid oscillations in the densities.

The SKX and SKM* interactions can be used to calculate charge densities for other nuclei including those which could be studied in radioactive beam experiments. Comparison with experiment will provide a test of the mean-field models and for the orbit occupancies in situations of more extreme neutron-to-proton ratios than those found in stable nuclei. These charge densities are also important as input to precise electronic structure calculations [41]. For nuclei with $N=Z$, the neutron and proton densities are essentially equal (the rms radius for protons is 1–2 % larger than for neutrons due to the repulsive Coulomb interaction); but for nuclei with a neutron excess, there is a larger theoretical uncertainty which can be related to the uncertainty in the pressure of the neutron equation of state [42–44]. Elastic proton scattering at medium energy analyzed in terms of microscopic proton-nucleus interaction models provides perhaps the best test for the shape and size of the neutron density [45].

ACKNOWLEDGMENTS

We thank Dr. M. Honma for providing the occupation numbers for some pf-shell nuclei obtained with the FPD6 interaction. Support for this work was provided from the U.S. National Science Foundation Grant No. PHY-007091 and the South African National Research Foundation.

[1] H. de Vries, C.W. de Jager, and C. de Vries, At. Data Nucl. Data Tables **36**, 495 (1987).
[2] G. Fricke, C. Bernhardt, K. Heilig, L.A. Schaller, L. Shellenberg, E.B. Shera, and C.W. de Jager, At. Data Nucl. Data Tables **60**, 177 (1995).
[3] B.A. Brown, S.E. Massen, and P.E. Hodgson, Phys. Lett. **85B**, 167 (1979); J. Phys. G **5**, 1655 (1979).
[4] R.E. Julies, W.A. Richter, and B.A. Brown, S. Afr. J. Phys. **15**, 35 (1992).
[5] B.A. Brown and B.H. Wildenthal, Annu. Rev. Nucl. Part. Sci. **38**, 29 (1988).
[6] W.A. Richter, M.G. Van der Merwe, R.E. Julies, and B.A. Brown, Nucl. Phys. **A523**, 325 (1991).
[7] X. Ji and B.H. Wildenthal, Phys. Rev. C **37**, 1256 (1988).
[8] J. Blomqvist, L. Rydstrom, R.J. Liotta, and C. Pomar, Nucl. Phys. **A423**, 253 (1984); L. Rydstrom, J. Blomqvist, R.J. Liotta, and C. Pomar, *ibid.* **A512**, 217 (1990).
[9] B.A. Brown, W.A. Richter, and R. Lindsay, Phys. Lett. B **483**, 49 (2000).
[10] J. Bartel, P. Quentin, M. Brack, C. Guet, and M.B. Hakansson, Nucl. Phys. **A386**, 79 (1982).
[11] B.A. Brown, Phys. Rev. C **58**, 220 (1998).
[12] A.E.L. Dieperink and P.K.A. de Witt Huberts, Annu. Rev. Nucl. Part. Sci. **40**, 239 (1990).
[13] C. Mahaux, P.F. Bortignon, R.A. Broglia, and C.H. Dasso, Phys. Rep. **120**, 1 (1985).
[14] W. Kohn and L.J. Sham, Phys. Rev. **140**, A1133 (1965); R. M. Dreizler and E. K. U. Gross, *Density Functional Theory: An Approach to the Quantum Many-Body Problem* (Springer, Berlin, 1990).
[15] B. Dreher, J. Friedrich, K. Merle, H. Rothhaas, and G. Luhrs, Nucl. Phys. **A235**, 219 (1974).
[16] B. Dreher, Phys. Rev. Lett. **35**, 716 (1975)
[17] P.G. Reinhard, J. Friedrich, and N. Voegler, Z. Phys. A **316**, 207 (1984).
[18] B.A. Brown, S. Typel, and W.A. Richter, Phys. Rev. C **65**, 014612 (2002).
[19] H. Miessen, Ph.D. thesis, University of Mainz, 1982.
[20] D. Rychel, Ph.D. thesis, University of Mainz, 1983.
[21] J. Wesseling, C.W. de Jager, L. Lapikas, H. de Vries, L.W. Fagg, M.N. Harakeh, N. Kalantar-Nayestanaki, R.A. Lindgren, E. Moya De Guerra, and P. Sarriguren, Phys. Rev. C **55**, 2773 (1997)
[22] H. J. Emrich, Ph.D. thesis, University of Mainz, 1983.
[23] J.W. Lightbody, Jr., J.B. Bellicard, J.M. Cavedon, B. Frois, D. Goutte, M. Huet, Ph. Leconte, A. Nakada, Phan Xuan Ho, S.K. Platchkov, S. Turck-Chieze, C.W. de Jager, J.J. Lapikas, and P.K.A. de Witt Huberts, Phys. Rev. C **27**, 113 (1983)

[24] H. D. Wohlfahrt, Habilitationsschrift, University of Mainz, 1976.
[25] G. Beuscher, Ph.D. thesis, University of Mainz, 1983.
[26] G. Stephan, Ph.D. thesis, University of Mainz, 1976.
[27] H. Rothhaas, Ph.D. thesis, University of Mainz, 1976.
[28] A. J. C. Burghardt, Ph.D. thesis, University of Amsterdam, 1989.
[29] H. Euteneuer, J. Friedrich, and N. Vögler, Nucl. Phys. **A298**, 452 (1978).
[30] J. L. Friar, J. Heisenberg, and J. W. Negele, in *Proceedings of the June Workshop in Intermediate Energy Electromagnetic Interactions*, edited by A. M. Bernstein (MIT, Cambridge, MA, 1977), p. 325.
[31] B.A. Brown, C.R. Bronk, and P.E. Hodgson, J. Phys. G **10**, 1683 (1984).
[32] J.W. Negele and D.O. Riska, Phys. Rev. Lett. **40**, 1005 (1978).
[33] M. Honma, T. Otsuka, B.A. Brown, and T. Mizusaki, Phys. Rev. C **65**, 061301 (2002).
[34] L. Bennour, P.H. Heenen, P. Bonche, J. Dobaczeswki, and H. Flocard, Phys. Rev. C **40**, 2834 (1989).
[35] R.J. Furnstahl and C.E. Price, Phys. Rev. C **44**, 895 (1991).
[36] V.J. Pandharipande, I. Sick, and P.K.A. deWitt Huberts, Rev. Mod. Phys. **69**, 981 (1997).
[37] G.J. Kramer, H.P. Blok, and L. Lapikas, Nucl. Phys. **A679**, 267 (2001).
[38] J.M. Udias, P. Sarriguren, E. Moya de Guerra, E. Garrido, and J.A. Caballero, Phys. Rev. C **48**, 2731 (1993).
[39] E.N.M. Quint, J.F.J. van den Brand, J.W.A. den Herder, E. Jans, P.H.M. Keizer, L. Lapikas, G. van der Steenhoven, P.K.A. de Witt Huberts, S. Klein, P. Grabmayr, G.J. Wagner, H. Nann, B. Frois, and D. Goutte, Phys. Rev. Lett. **57**, 186 (1986).
[40] P. Grabmayr, A. Mondry, G.J. Wagner, P. Woldt, G.P.A. Berg, J. Lisantti, D.W. Miller, H. Nann, and E.J. Stephenson, Phys. Rev. C **49**, 2971 (1994).
[41] D. Andrae, Phys. Rep. **336**, 413 (2000).
[42] B.A. Brown, Phys. Rev. Lett. **85**, 5296 (2000).
[43] S. Typel and B.A. Brown, Phys. Rev. C **64**, 027302 (2001).
[44] R.J. Furnstahl, Nucl. Phys. **A706**, 85 (2002).
[45] S. Karataglidis, K. Amos, B.A. Brown, and P.K. Deb, Phys. Rev. C **65**, 044306 (2002).